



Simulation of a soft-gamma-ray polarimeter on board a microsatellite

Xiang-Man Liu^{1,2,3} · Shu-Wen Tang^{1,2} · Wei Wang^{4,5} · Yu-Hong Yu^{1,2} · Zhi-Yu Sun^{1,2} · Yong-Jie Zhang^{1,2} · Fang Fang^{1,2} · Duo Yan^{1,2} · Shi-Tao Wang^{1,2} · Xue-Heng Zhang^{1,2} · Shu-Ya Jin^{1,2} · Bi-Tao Hu³

Received: 4 March 2023 / Revised: 8 June 2023 / Accepted: 9 July 2023 / Published online: 14 November 2023

© The Author(s), under exclusive licence to China Science Publishing & Media Ltd. (Science Press), Shanghai Institute of Applied Physics, the Chinese Academy of Sciences, Chinese Nuclear Society 2023

Abstract

Gamma-ray polarimetry is a new and prospective tool for studying extremely high-energy celestial objects and is of great significance for the field of astrophysics. With the rapid development of microsatellite technology, the advantages of space exploration have become increasingly apparent. Therefore, we simulated a soft-gamma-ray polarimeter for a microsatellite based on the Compton scattering principle. We performed detailed Monte Carlo simulations using monoenergetic gamma-ray linear-polarization sources and Crab-like sources in the energy range of 0.1–10 MeV considering the orbital background. The polarimeter exhibited excellent polarization detection performance. The modulation factor was 0.80 ± 0.01 , and the polarization angles were accurate within an error of 0.2° at 200 keV for on-axis incidence. For the Crab-like sources for on-axis incidence, the polarization degrees were consistent with the set values within the error tolerance, the modulation factor was 0.76 ± 0.01 , and the minimum detectable polarization reached 2.4% at 3σ for an observation time of 10^6 s. Additionally, the polarimeter exhibited recoil electron tracking, imaging, and powerful background suppression in a large field of view (FoV; $\sim 2\pi$ sr). The proposed polarimeter meets the requirements of a space soft-gamma-ray polarization detector and has promising research prospects.

Keywords Soft gamma ray · Polarization · Compton scattering · Microsatellite · Monte Carlo simulation

This work was supported by the National Natural Science Foundation of China (Nos. U2031206, 12273086, 12133007) and the CAS Key Technology Talent Program.

✉ Shu-Wen Tang
tangsw@impcas.ac.cn

✉ Wei Wang
wangwei2017@whu.edu.cn

¹ Institute of Modern Physics, Chinese Academy of Sciences, Lanzhou 730000, China

² School of Nuclear Science and Technology, University of Chinese Academy of Sciences, Beijing 100049, China

³ School of Nuclear Science and Technology, Lanzhou University, Lanzhou 730000, China

⁴ Department of Astronomy, School of Physics and Technology, Wuhan University, Wuhan 430072, China

⁵ Wuhan University-National Astronomical Observatories Joint Center for Astronomy, Wuhan University, Wuhan 430072, China

1 Introduction

Gamma-ray polarization measurement in gamma-ray astronomy is broadly considered a new and powerful diagnostic tool for addressing open questions about the most extreme high-energy sources. This includes gamma-ray bursts (GRBs), pulsars, active galactic nuclei (AGNs), and binary black holes (BBHs) [1, 2], which may not be resolved or explained through the timing, energy, and direction of gamma rays. In GRB studies, polarization measurements can illuminate the nature of the central engines that produce ultra-relativistic jets in GRBs as well as the physical properties, radiation mechanisms, and energy dissipation points of these jets. They also contribute to the constraints of the theoretical models about the origin of GRBs [1, 3–6]. Detecting the gamma-ray polarization emitted by pulsars can help estimate the magnetic field structure around compact objects, understand the mechanism of gamma-ray emission (curvature radiation or synchrotron radiation), and predict particle acceleration and pair-cascading processes in the magnetosphere of pulsars [1, 7]. In particular, accreting black hole (BH) systems, including BBHs and AGNs, are

considered to radiate linearly polarized X-rays and gamma rays owing to the scattering processes in their accretion disks; therefore, the measurement of these polarization features will allow us to identify the geometry of the corona [2, 8]. Additional examples of space gamma-ray polarization as a unique tool for studying high-energy astrophysics can be found in Refs. [9–13]. In conclusion, gamma-ray polarization is a valuable upcoming tool for astrophysical studies, making space gamma-ray polarization measurements extremely attractive.

Under the tremendous scientific lure of space gamma-ray polarization, many astrophysicists worldwide have joined teams to detect space gamma-ray polarization and have made efforts in polarization detection by launching satellites and flying high-altitude balloons. A few typical polarization-related satellite experiments include the X-ray polarimeter on board the eighth Orbiting Solar Observatory (OSO-8) mission [14], the Ramaty High-energy Solar Spectroscopic Imager mission [15], IBIS and SPI on board the International Gamma-ray Astrophysics Laboratory [12, 16], and the Gamma-Ray Burst Polarimeter on board the IKAROS spacecraft [17], POLAR placed on the Chinese space station TG-2 [18], and the Cadmium Zinc Telluride Imager on board the ASTROSAT satellite [19]. Besides the abovementioned satellite experiments, representative balloon experiments include the Polarimeter for High-Energy X-rays [20], the Polarized Gamma-ray Observer (PoGO) [21], PoGO+ [22], the Gamma-ray Polarimeter Experiment [23], and the Gamma-Ray Astro-Imager with Nuclear Emulsion experiment [24]. Although the number of polarization detection experiments available is relatively large, most are focused on the X-ray band, especially the hard X-ray band (tens to hundreds of keV). Only a few of these experiments have been able to detect high-energy (>10 MeV) gamma-ray polarization, while polarization detection in the soft-gamma-ray band (~ 0.1 – 10 MeV), especially above 1 MeV, is sorely lacking.

In general, the most efficient method for detecting the polarization of soft gamma rays is based on the Compton scattering principle. This is because the radiation physics processes from the interaction of soft gamma rays with matter are dominated by Compton scattering. Similarly, low- and high-energy gamma-ray polarization is dominated by the photoelectric effect and the electron–positron pair production, respectively. A medium-energy gamma-ray astronomy (MEGA) telescope [25], based on the Compton scattering principle, can detect soft-gamma-ray polarization. Unfortunately, the MEGA project has not been completed yet for various reasons. The Compton Spectrometer and Imager (COSI) [26], which is also based on the Compton scattering principle, is equally sensitive to gamma-ray polarization in this energy band. However, COSI is only an end-of-flight balloon experiment and faces many challenges (e.g.,

atmospheric absorption, scattering, and limited exposure) in gamma-ray polarization detection as a balloon payload. This significantly reduces the ability of the detector to detect soft-gamma-ray polarization in space. The best solution is to send the detector to space by launching a detection satellite. Given the above analysis, there is a need for a satellite soft-gamma-ray polarimeter to occupy this almost empty energy region, which is of great scientific importance in astrophysical research.

Undoubtedly, the best way to measure gamma-ray polarization in the universe is through satellite detection. With the advances in science and technology, the development of modern small satellites has become increasingly rapid and offers advantages such as small size, light weight, high technology, short development cycle, low cost, standardized stars, modular design technology, mass production and storage in the flow line, and ease of launch [27, 28]. Compared with modern small satellites, traditional exploration satellites have apparent disadvantages such as large size and weight, complex technology, long development period, high cost, high risk, and difficulty in achievement [27, 28]. Thus, modern small satellites provide a new perspective on cosmic gamma-ray polarimetry.

To achieve a high-precision all-sky survey of the polarization of soft gamma rays in space, we can use a constellation composed of multiple microsattellites, such as the “GRID mission” [29]. Excellent polarization detection performance is essential for each microsattellite in a constellation. Therefore, in this study, a detailed investigation was conducted on a microsattellite (polarimeter), and a novel detector design based on the principle of Compton scattering was proposed to detect the linear polarization of soft gamma rays. Moreover, a detector mass model was constructed, and a detailed Monte Carlo simulation was implemented to verify the model performance. As demonstrated by the simulation results, the designed polarimeter exhibited excellent performance. Overall, this study validates the rationality of the proposed detector design scheme, lays a solid foundation for future polarimeter development, and offers a meaningful reference for other researchers to design and develop detection satellites.

2 Principles and methods

2.1 Principle of polarization measurement

In the soft-gamma-ray domain, Compton scattering is the dominant process in photon–matter interaction. Compton scattering preserves the polarization information of the linearly polarized photons to a certain degree. When linearly polarized photons and matter undergo Compton scattering, the azimuthal angle distribution of the scattered photons is related to the

degree of polarization and the direction of polarization of the incident photons. The soft-gamma-ray polarimeter used in this study was based on this principle to detect gamma-ray polarization signals in the universe.

If the initial gamma ray is linearly polarized, Compton scattering can be graphically demonstrated, as shown in Fig. 1. Additionally, the Compton scattering differential cross section of a linearly polarized photon can be expressed by the Klein–Nishina formula [18]

$$\begin{aligned} \frac{d\sigma}{d\Omega} &= \frac{r_0^2}{2} \left(\frac{E'}{E}\right)^2 \left(\frac{E}{E'} + \frac{E'}{E} - 2 \sin^2 \theta \cos^2 \eta\right) \\ &= \frac{r_0^2}{2} \left(\frac{E'}{E}\right)^2 \\ &\left\{ \frac{E}{E'} + \frac{E'}{E} - \sin^2 \theta + \sin^2 \theta \cos \left[2\left(\eta + \frac{\pi}{2}\right)\right] \right\}, \end{aligned} \tag{1}$$

where r_0 is the classical electron radius, E is the incident or initial photon energy, E' is the scattered photon energy, θ is the Compton scattering angle, and η is the angle between the direction of the scattered photon and the polarization direction of the incident photon (i.e., the azimuthal angle), as shown in Fig. 1. E'/E in Eq. (1) is represented by the Compton equation [1]

$$\frac{E'}{E} = \left[1 + \frac{E}{m_e c^2} (1 - \cos \theta) \right]^{-1}, \tag{2}$$

where $m_e c^2$ denotes the rest mass energy of an electron. Equation (1) indicates that linearly polarized photons tend to scatter perpendicularly to the incident polarization

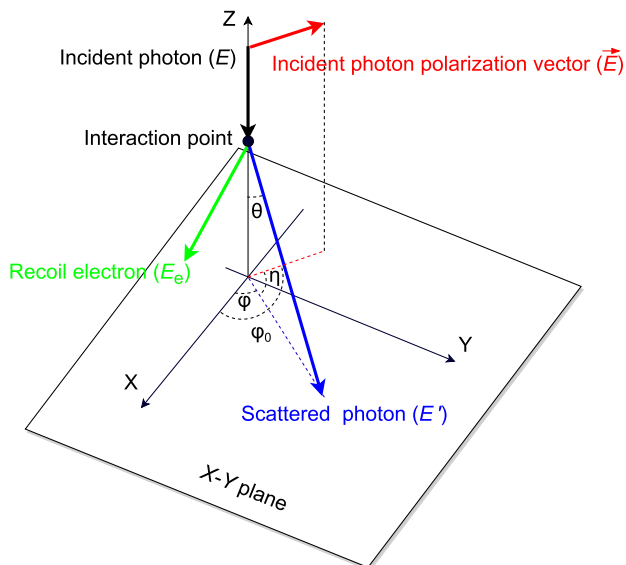


Fig. 1 (Color online) Schematic of Compton scattering of a linearly polarized photon. (Color figure online)

vector (minimizing the term $2 \sin^2 \theta \cos^2 \eta$). Additionally, when both E'/E and θ are constants, the differential scattering cross section of the polarized photons follows the $\cos[2(\eta + \pi/2)]$ distribution, that is, the variation in the number of scattered photons with the azimuthal angle η follows the cosine distribution. In practice, the incident photon energy E and scattering angle θ often take a range of values; our measurement is an average, but the averaged azimuth still follows a cosine distribution.

In most cases, because η cannot be measured directly, the polarization information of the incident linearly polarized photons cannot be obtained by measuring η . Given the above practical situation, the angle φ is introduced as the Compton scattering azimuth, which is the angle between the polarized scattered photon plane and the x-axis, as shown in Fig. 1. The polarization signatures of the source of incident linearly polarized photons are reflected in the distribution of the azimuthal angle φ :

$$f(\varphi) = A \{ 1 + \mu \cos [2(\varphi - \varphi_0) + \pi] \}, \tag{3}$$

which can easily be deduced from Eq. (1). Here, φ_0 represents the polarization angle of the incident photon or the direction of the original polarization vector (see Fig. 1), A is the offset of the distribution of the azimuthal scatter angle (see Fig. 2), and μ is a significant parameter called the modulation factor, which describes the polarization response of a polarimeter. The modulation curve derived by Eq. (3) is shown in Fig. 2. The modulation factor μ is expressed as:

$$\mu = \frac{F_{\max} - F_{\min}}{F_{\max} + F_{\min}} = \frac{B}{A} = \frac{\sin^2 \theta}{\frac{E'}{E} + \frac{E}{E'} - \sin^2 \theta}, \tag{4}$$

which can be derived from Eqs. (1), (2), and (3), where F_{\max} , F_{\min} , A , and B are presented in Fig. 2. For a fully (100%) linearly polarized photon beam, the modulation factor is μ_{100} ,

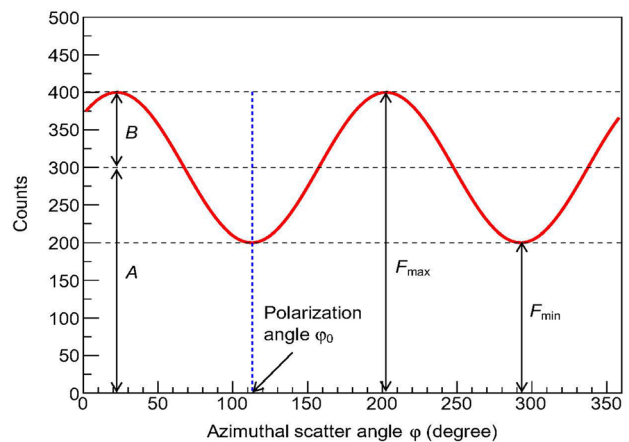


Fig. 2 (Color online) Distribution of the azimuthal scatter angle φ

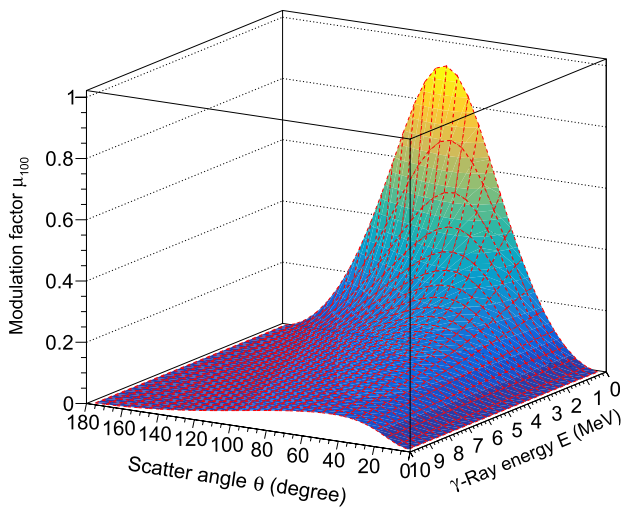


Fig. 3 (Color online) Modulation factor μ_{100} as a function of the Compton scattering angle θ and the incident photon energy E

whereas for a photon beam of an unknown degree of polarization, the modulation factor is μ . The degree of polarization of the incident photons can be obtained as:

$$P = \frac{\mu}{\mu_{100}}, \tag{5}$$

where P is a positive value between 0 and 1.

Figure 3 illustrates the relationship (the functional relationship expressed by Eq. (4)) among the modulation factor μ_{100} , which is a key performance parameter of the polarimeter, the Compton scatter angle θ , and the incident photon energy E . As shown in Fig. 3, the modulation of the azimuthal distribution is most significant at lower energies and medium scattering angles. Photons with extremely large ($\theta \approx 180^\circ$) or small ($\theta \approx 0^\circ$) scattering angles carry little polarization information. Additionally, the modulation factor μ_{100} decreases significantly with an increase in the photon energy.

In addition to the modulation factor, the minimum detectable polarization (MDP; also known as polarization sensitivity, i.e., the detection limit of the degree of polarization [30]) describes the performance of a polarimeter. MDP is used to determine the polarization detection capability of a polarimeter and can be calculated as [1]:

$$MDP = \frac{n_\sigma}{\mu_{100}S} \sqrt{\frac{S+B}{T}}, \tag{6}$$

where n_σ is related to the expected confidence level of the detection (e.g., $n_\sigma = 3$) and S and B are the count rates of the source and background (after all event selection cuts are applied) in observation time T , respectively. As can be seen from Eq. (6), MDP is related to five parameters. In

general, n_σ , μ_{100} , and T are constants when the confidence level, polarimeter, and observation time are fixed. Thus, the MDP is only affected by S and B , and the MDP improves with increasing S and worsens with increasing B . Given that the angular resolution is used as the key event selection condition when calculating S and B , S and B are related to the angular resolution of the detector. In fact, the excellence of the angular resolution has almost no effect on S , whereas it has a significant effect on B . When the angular resolution is excellent, B decreases, which results in better MDP for the polarimeter. In contrast, when the angular resolution is poor, B increases, which leads to worse MDP for the polarimeter. Therefore, the angular resolution significantly affects the polarization sensitivity of a polarimeter, which provides a valuable guide for the design of polarimeters.

2.2 Polarimeter design

In this study, a polarimeter was designed to detect the polarization of linearly polarized gamma rays in the energy range of 0.1–10 MeV based on the Compton scattering principle. The structural design of the proposed polarimeter is illustrated in Fig. 4, where the entire model contains only active materials. The polarimeter is mainly composed of three detection subsystems: a silicon converter (blue) located in the upper center of the polarimeter, a CsI absorber (red) surrounding the converter on five sides (except for the top side), and an organic plastic scintillator anticoincidence shield (ACS; green), which envelops the two subdetectors mentioned above. The entire detector containing only the sensitive material has a size of 26 cm \times 26 cm \times 20 cm and a mass of \sim 15 kg. The design details and descriptions of each subdetector of the polarimeter are given below.

Converter The converter plays a vital role in the polarimeter and performs two main tasks: (1) the first Compton interaction occurs in the converter and (2) the converter records the deposited energy and interaction positions of all

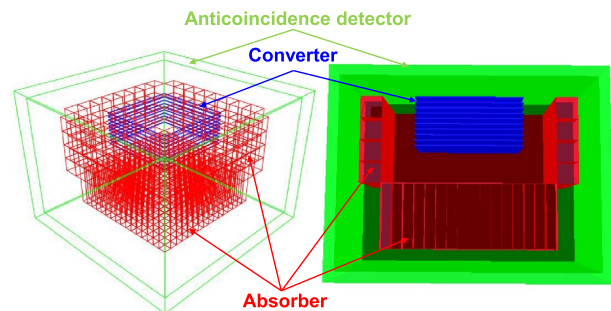


Fig. 4 (Color online) Wireframe model (left) and mass model (right) of the polarimeter, which consists of the outer organic plastic scintillator anticoincidence shield (green), a silicon converter (blue) located in the upper middle, and a CsI absorber (red) surrounding the five sides of the converter

Table 1 Design parameters of each subdetector of the polarimeter

Subdetector	Design shape	Sensitive materials	Total mass (kg)	Cell size (cm ³)	Number of cells	Photon absorption probability @ 1 MeV (%)	Layer spacing (cm)	Number of strips on a cell and strip pitch
Converter	Multi-layer array	Silicon	~0.2	10×10×0.1	10	~15	0.5	50, 2 mm
Absorber	Pixel-type array	CsI	~11.5	Bar:1×1×6 Cube:2×2×2	Bar:256 Cube:128	Bar:~80 Cube:~42	–	–
ACS	Hollow shell	Organic plastic scintillator	~3.3	26×26×20, thickness:1 cm	1	–	–	–

generated particles. To accomplish these tasks, the converter is required to be able to increase the Compton scattering probability of photons, stop recoil electrons, and have excellent energy and position resolution. A multilayer double-sided silicon strip detector was found to be the best converter design choice. Silicon, a low-*Z* material, has a higher Compton cross section than medium-*Z* and high-*Z* materials such as Ge and CdZnTe in the 0.1–10 MeV energy range. The double-sided silicon strip detector has a low threshold and guarantees excellent energy and two-dimensional (i.e., in the *X*- and *Y*-directions) position resolution. Furthermore, multiple thin-layer configurations can enlarge the Compton scattering cross section, provide longitudinal position information, and track and absorb recoil electron energy. The geometric model of the converter and its physical location in the system are shown in blue in Fig. 4. The detailed design parameters are listed in Table 1.

Absorber The absorber (also known as the calorimeter) is required to stop the scattered Compton photons and measure their energy and position. Additionally, because Compton scattering polarization is significant at larger scattering angles and lower energies, the absorber must be able to measure large-angle-scattered photons. Finally, the absorber acts as a barrier to reduce the radiation from the space-orbit environment to the converter and improve the background rejection of the entire detector. Therefore, the absorber that meets these requirements needs to use high-*Z* materials as the detection medium, have good energy and position resolution, have a large acceptance of scattered photons, and surround the converter as much as possible. The CsI scintillator is a better choice as a sensitive material for the absorber because of its high density, large atomic number, high light yield, good mechanical properties, not easily deliquescent, high detection efficiency, ease of processing into small pixels of various shapes, availability in large quantities, and reasonable price [31]. A pixel-type absorber comprising CsI crystals was used as the final solution. Two types of crystal cells were used: cubic and bar shaped. The geometric configuration of the absorber and its physical position in the

system are shown in red in Fig. 4. The design parameters are listed in Table 1.

Considering the power consumption and space constraints of a compact microsatellite, we adopted silicon photomultipliers (SiPMs) as the photoelectric converters for CsI crystals instead of traditional photomultiplier tubes (PMTs). SiPMs have low power consumption, low weight, small size, fast time response, large self-gain (10^5 – 10^6), high signal-to-noise ratio, and insensitivity to magnetic fields [29, 32]. Each small cubic crystal coupled the photoelectric converter only on the side facing away from the silicon converter to minimize the passive material between the converter and the absorber. A dual-ended readout scheme was used for the bar crystals. To verify the feasibility of this scheme, we conducted a detailed test study on a CsI detection cell in the laboratory (see Refs. [31, 33]). The experimental results showed that the CsI detection cell exhibited good performance; the energy resolution was close to 5% (full width at half maximum; FWHM), and the longitudinal position resolution was approximately 5 mm (FWHM) for the 662 keV gamma-ray emitted by the ¹³⁷Cs source. The dual-ended readout method not only ensures better energy resolution but also provides position information along the crystal bar direction (*Z*-direction).

ACS The ACS of the polarimeter is primarily used to prevent background events induced primarily by charged particles (e.g., protons, alphas, electrons, and positrons) in the orbital environment in space (described in Sect. 2.4). A shell-shaped hollow plastic scintillator with a thickness of 1 cm was used as an anticoincidence shield to completely cover the converter and absorber. The green part in Fig. 4 shows the geometric configuration of the ACS and its physical location in the entire system. Some of the design parameters are listed in Table 1.

2.3 Simulation and analysis tools

The Medium Energy Gamma-ray Astronomy library (MEG-Alib) [34] is an open-source Monte Carlo simulation and data analysis package that is entirely written in C++ and

based on ROOT [35] and Geant4 [36]. It was explicitly designed for gamma-ray detectors in the low-to-medium-energy region. It can be used for the design of detector geometry and simulation of the interaction process of gamma rays and other particles with matter, as well as for data analysis. The reliability of the MEGALib package for the simulation and data analysis of low- and medium-energy gamma-ray detectors has been recognized by researchers in this field. MEGALib has been successfully applied to various hard X-ray/gamma-ray telescope projects and studies in space and on the ground, such as MEGA [37], COSI [26], AMEGO [38], COMPTEL [39], ACT [40], TIGRE [41], e-ASTROGAM [7], and a combined Compton and coded-aperture telescope for medium-energy gamma-ray astrophysics [42].

The simulation of a detector based on MEGALib first requires the creation of a realistic geometry using the Geomega package contained in MEGALib [34, 37, 41], as shown in Fig. 4. The geometry includes the shape, size, location, material, and properties of the surrounding environment for each volume that constitutes the detector. The cosmic simulator Cosima, integrated with the MEGALib package, was used to perform Monte Carlo simulations [34, 37, 41]. Cosima can combine Geant4 and a specified source to simulate particle transport and interaction with geometric materials and then generate an output file that stores the simulated interaction information. Simulation data analysis was performed using Revan and Mimrec contained in MEGALib [34, 37, 41, 43]. We then obtained the simulation results. Additionally, MEGALib uses background data generated by the LEOBackground software package [44], which is written entirely in Python, to simulate the low-earth orbit (LEO) environment. The above is only a brief overview of the functions of the main subpackages of MEGALib (for a detailed description and usage see Refs. [34, 37, 41, 43, 44]).

2.4 Simulation method

Currently, simulation experiments are the primary methods used to investigate the performance of our polarimeter. In this section, we detail the polarimeter simulation method, including an overview of the simulation experiment flow, a detailed configuration of the performance parameters of each subdetector, a configuration of the particle sources (gamma-ray sources and background sources), and a brief data analysis process.

Figure 5 shows a brief flowchart of our simulation experiments using the MEGALib package. First, a realistic geometric model of the detector was constructed, and reasonable performance parameters were set for the detector to adapt the simulation to reality. Additionally, the gamma rays and background sources were configured. Note that along with the particle sources configuration, items such as the

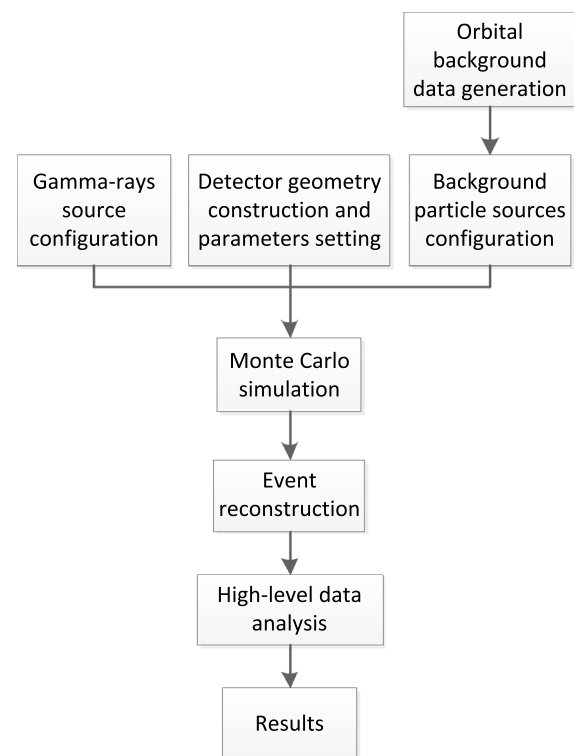


Fig. 5 Brief flow of simulation experiments using MEGALib. (Color figure online)

physics lists, data output formats, data storage files, and simulation stop conditions were also set. Next, Geant4 was called by MEGALib to complete the Monte Carlo simulation. The simulated data were then reconstructed (i.e., Compton event reconstruction) using the proven event reconstruction algorithm in MEGALib. Finally, the simulation results were obtained after a high-level analysis of the reconstructed events using MEGALib.

A realistic geometric model of the polarimeter, constructed using the MEGALib package, is shown in Fig. 4 and described in detail in Sect. 2.2. To ensure that the simulation results accurately reflect the condition of the detector, the setting of the simulation parameters is crucial. Reasonable parameters can provide more realistic and reliable results regarding the performance of the detector obtained by the simulation experiment. The double-sided silicon strip detectors comprising the converter were assumed to have a uniform energy resolution of 10 keV FWHM, a noise threshold of 15 keV, and a trigger threshold of 30 keV [37]. The position resolution of the converter was determined by the number of strips and the thickness of each silicon wafer (as described in Sect. 2.2). For the CsI absorber, energy resolutions of 15% FWHM at 100 keV, 9% FWHM at 350 keV, 6.5% FWHM at 511 keV, 5% FWHM at 662 keV, 3.5% FWHM at 1000 keV, and 2.7% FWHM at 5000 keV were set. Furthermore, a noise threshold of 30 keV and a trigger

threshold of 50 keV were selected [31, 33, 37]. The depth resolution (Z -direction) of the 6 cm CsI crystal was assumed to be 0.5 cm FWHM [31, 33], but no depth resolution was provided for the 2-cm cubic crystal. Additionally, the geometry of the crystals determined their spatial resolution; the specific parameters are described in Sect. 2.2. The organic plastic scintillator ACS used an energy resolution of 10 keV (1σ Gaussian), a trigger threshold of 100 keV, and a detection efficiency of 99.9% for the charged particles.

Because the MEGALib package provides the function of user-defined particle sources, we can flexibly set the particle sources for the simulation according to our requirements. For our purposes, we used a monochromatic, negative power law, and file format (generated by the LEOBackground software package) for the energy spectrum, as well as beam parameters for the far-field point source (i.e., homogeneous beam) and far-field area source. When setting up the particle sources, we considered the fact that far-field sources are so far away that they arrive at the detector in the form of plane waves. Three types of sources were used in our simulation experiments. First, a monochromatic homogeneous beam with a flux of 1.0 ph/cm²/s was simulated and used to irradiate a polarimeter mass model. The polarization response of the polarimeter was studied by varying the energy, angle, and polarization direction of the incident photons. Next, the homogeneous beam was repeated using a power-law energy spectrum to simulate a discrete celestial source of linearly polarized gamma rays (i.e., a Crab-like source). For the Crab-like source, events were generated by linearly polarized and unpolarized photon beams with an energy spectrum of $4 \times 10^{-3} E^{-2}$ ph/cm²/s/MeV between 0.1 and 10 MeV [45]. A simulation experiment was performed using this type of source to investigate the polarization response of the polarimeter to realistically polarized photons and its polarization performance. Third, an isotropic beam source (i.e., a far-field area source) with the spectrum in file form was constructed and used to simulate the space-orbit environment. Because the polarimeter is expected to complete a satellite mission, the impact of the complex space-orbit environment on the detector should be considered. The background environment depends largely on the orbit in which the satellite operates. In this case, a typical LEO with an altitude of 550 km and an inclination of 0° was selected. The detection of the corresponding orbital background environments by the BeppoSAX [46] and AGILE [47] missions has made orbital background environments such as this one well-known. Figure 6 shows the background environment used in the polarimeter simulation experiments, which was calculated and provided by the LEOBackground software package. The background components in Fig. 6 consist of cosmic and albedo photons, hadrons (e.g., neutrons, protons, and alphas), and leptons (e.g., electrons and positrons). The energy spectra in the file

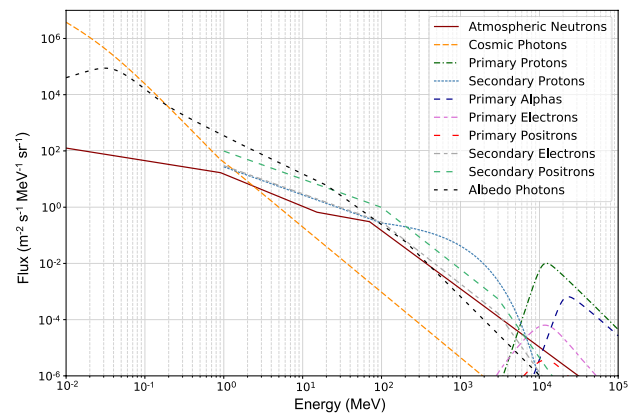


Fig. 6 (Color online) Background environment of the polarimeter on an orbit with an altitude of 550 km and a 0° inclination

form used for the simulation experiments were the background energy spectra.

For the data analysis, a coincident event filter was first adopted to select events that satisfied at least one hit in the converter and at least one hit in the absorber. Next, the Compton sequence reconstruction (CSR) algorithm with trajectory tracking [37] was applied to the selected events for Compton event reconstruction, which requires the first hit of the event to occur in the converter. Information related to the incident photon, such as its initial energy, incident direction, and scattering angle, can then be obtained. The above were performed by Revan in MEGALib. The event selection method ensures the integrity of Compton events and plays a vital role in reducing background events. Finally, the reconstructed events were further processed and analyzed using the Mimrec tool in MEGALib, including event cuts, plotting of the reconstructed energy spectrum, evaluation of the angular resolution measurement (ARM), specified as the angular distance between a known source position and the closest reconstructed position on the Compton cone, calculation and correction of modulation curves, and image reconstruction. When we analyzed the reconstructed events, we adopted the same fixed event cuts for events generated by monoenergetic photons, including a $\pm 3\sigma$ photopeak energy window and $\pm 3\sigma$ ARM cut. Moreover, there was a variable event cut, namely the scattering angle cut, which was adjusted according to the different photon energies, and the scattering angle window was roughly chosen between 40° and 110°. For events generated by Crab-like sources, both a $\pm 3\sigma$ ARM window and a [60°, 110°] Compton scattering angle window were applied as event cuts and no energy cut was used. The same event analysis method was used for events generated by background sources in the polarimeter. After data processing, the distribution of azimuthal scattering angles was obtained. The polarization information of the

incident photons was obtained from the parameters fitted to the azimuthal distribution.

3 Results and discussion

In the simulated experiments, various radiation physics processes occurred when soft gamma rays were incident on the polarimeter. These physical processes are primarily the photoelectric effect, Compton scattering (see γ_1 and γ_2 in Fig. 7), and electron–positron pair creation, where Compton scattering dominates. There are also cases where gamma rays do not interact with matter, such as $\gamma_3, \gamma_4,$ and γ_5 in Fig. 7. Since the proposed polarimeter is based on the Compton scattering principle for the detection of linearly polarized gamma rays, the Compton scattering process is of interest to us. We require that the incident gamma rays should satisfy the condition that they first undergo Compton scattering in the converter and are finally stopped by the absorber. The typical effective Compton scattering and detection processes of the polarimeter are described as follows. When a linearly polarized photon is incident on the polarimeter, it undergoes Compton scattering in a converter, which measures the position of the scattering point and the energy of the recoil electron. Further, the recoil electron can be tracked if it creates a trail in the converter. Then, the absorber absorbs the scattered photons and obtains the energy of the scattered photons and the position information of the absorption point. In some cases, recoil electrons escape the converter and are absorbed by the absorber (see γ_2 in Fig. 7), or photons undergo multiple Compton scattering before being completely stopped by the absorber (see γ_2 in Fig. 7). As shown in Fig. 7, γ_1 and γ_2 are valid events that satisfy the above conditions. The simulation results were obtained by analyzing valid events.

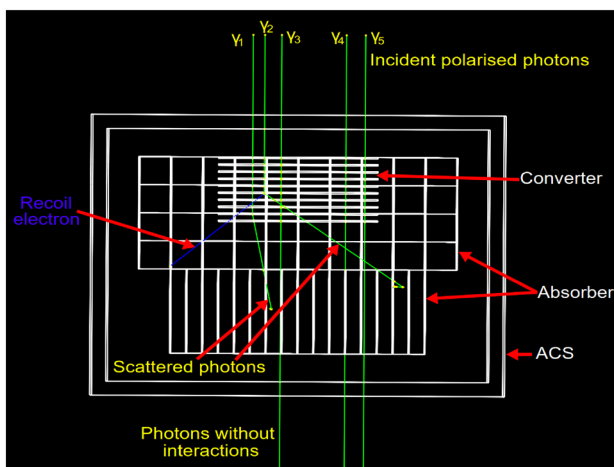


Fig. 7 (Color online) Interaction processes and traces left by gamma rays with an energy of 1000 keV incident on-axis into the polarimeter. To make the trajectory of the particles in the polarimeter clearer, we provide a front view of the detector

3.1 Polarization response to monoenergetic photons

Fully linearly polarized (100%) and non-polarized (0%) homogeneous on-axis photon beams with an energy of 200 keV were used in the simulation experiments; the other configuration parameters of both beams were identical (hereafter, photon beams are considered to be on-axis incidences unless otherwise specified). For a 100%-linearly polarized photon beam, the polarization vectors were (1, 0, 0). Raw azimuthal scatter angle distributions were obtained after analyzing the simulated data, as shown in Fig. 8. As shown in Fig. 8, the polarimeter responds to polarized photons (blue curve) more than unpolarized photons (black curve). However, although the blue curve approximately follows a cosine distribution, it is affected and distorted by systematic modulation owing to the nonuniformity of the detector; thus, the data might be difficult to fit using Eq. (3). Additionally, for the azimuthal angle distribution generated by the unpolarized photons in the detector (see the black curve in Fig. 8), an apparent spurious modulation (the black curve is not uniformly distributed) was observed owing to the nonuniformity of the detector response along the azimuthal angle (i.e., the effect of nonuniform response). Therefore, the raw azimuthal angle distribution must be corrected to eliminate the effect of systematic modulation on the modulation curve. To obtain the corrected azimuthal angle distribution, we use the following formula [2, 37]

$$f_{\text{cor}}(\varphi) = \frac{f(\varphi)}{f_{\text{non}}(\varphi)} \tag{7}$$

to correct the raw distribution. Here, $f(\varphi)$ is the raw azimuthal angle distribution generated by polarized photons (blue curve in Fig. 8), $f_{\text{non}}(\varphi)$ is the azimuthal angle distribution produced by unpolarized photons with the same

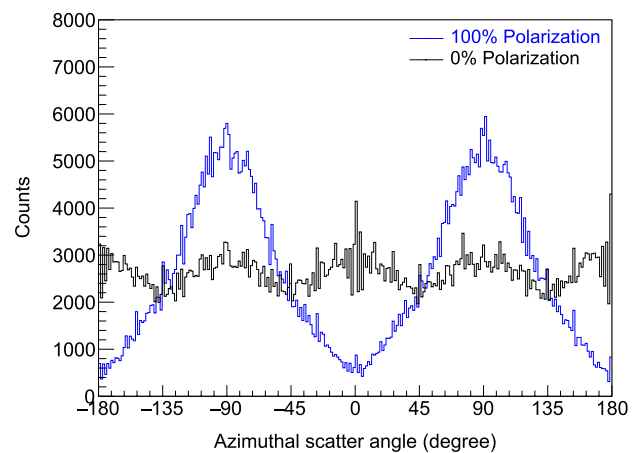


Fig. 8 (Color online) Raw azimuthal scatter angle distributions obtained from simulations for on-axis incidence of 100% (blue) and 0% (black) linearly polarized photon beams with energies of 200 keV

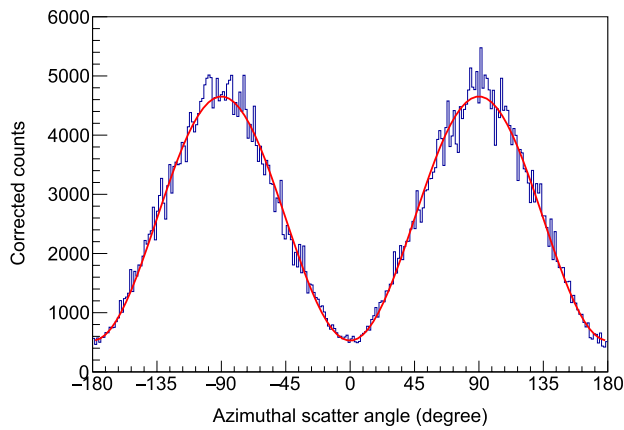


Fig. 9 (Color online) Azimuthal scatter angle distribution was obtained after the correction of the raw distribution (blue) in Fig. 8. The red curve was generated by fitting the corrected distribution using Eq. (3)

energy and incident direction as polarized photons (black curve in Fig. 8), and $f_{\text{cor}}(\varphi)$ is the corrected azimuthal angle distribution. Figure 9 presents the corrected modulation curve (hereafter, all the modulation curves shown and analyzed are corrected). Compared with the raw modulation curve (blue curve in Fig. 8), the corrected modulation curve follows the cosine distribution perfectly and can be fitted well by Eq. (3) (see Fig. 9). A modulation factor μ_{100} of 0.80 ± 0.01 was calculated using the fitting parameters. Furthermore, a polarization direction of the incident photons of $0.2^\circ \pm 0.2^\circ$ was obtained, which was in good agreement with the actual direction (0°). The simulation results demonstrate that the polarization response and performance of the polarimeter were excellent.

Figure 10 shows the corrected modulation curves fitted using Eq. (3) for four different polarization directions of a photon beam with an energy of 200 keV. The polarization parameters, such as the polarization angle and modulation factor of incident photons, for four different polarization directions were obtained and are listed in Table 2. The simulation results indicate that the polarimeter can precisely determine the polarization angle with an error of 0.2° , regardless of the change in the polarization direction of the incident photons.

During the data analysis, the Compton scattering events produced by polarized photons with an energy of 200 keV were selected with the Compton scattering angle as the filtering condition. The dependence of the modulation factor on the Compton scattering angle was also obtained. As shown in Fig. 11(a), the modulation factor is smaller for large and small scattering angles but increases significantly for medium scattering angles. Figure 11(b) shows the relationship between the energy of the incident polarized photons (100, 200, 300, 500, 800, 1000, 2000, 3000, 5000, and

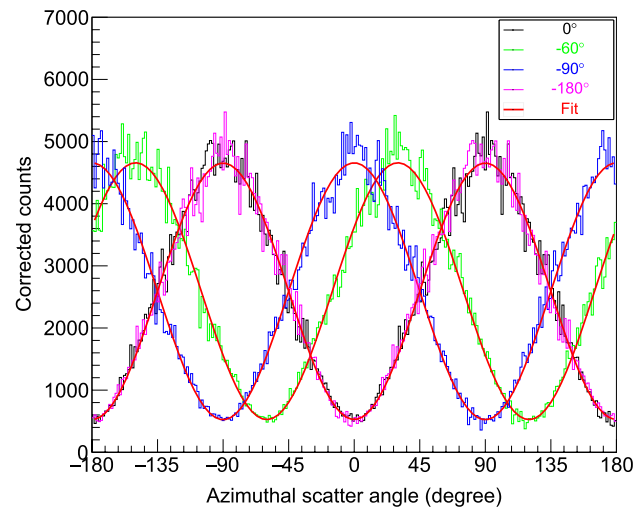


Fig. 10 (Color online) Corrected modulation curves and their best-fit curves (red). The polarization directions of the photon beams are 0° (black), -60° (green), -90° (blue), and -180° (magenta), respectively

Table 2 Polarization parameters for polarized photons with polarization directions of 0° , -60° , -90° , and -180°

Polarization direction setup (degree)	Polarization angle simulated (degree)	Modulation factor μ_{100} simulated
0	0.2 ± 0.2	0.80 ± 0.01
-60	-60.2 ± 0.2	0.80 ± 0.01
-90	-90.2 ± 0.2	0.80 ± 0.01
-180	-179.8 ± 0.2	0.80 ± 0.01

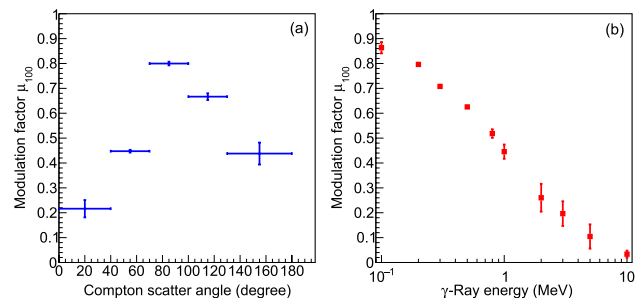


Fig. 11 (Color online) Dependence of the modulation factor on the Compton scattering angle (left panel, **a**) and the photon energy (right panel, **b**) for the monoenergetic photons

10000 keV) and the modulation factor, which is found to decrease with increasing incident photon energy. The simulation results are shown in Fig. 11. We conclude that the modulation of the azimuthal angle distribution is most significant at lower energies and medium Compton scattering

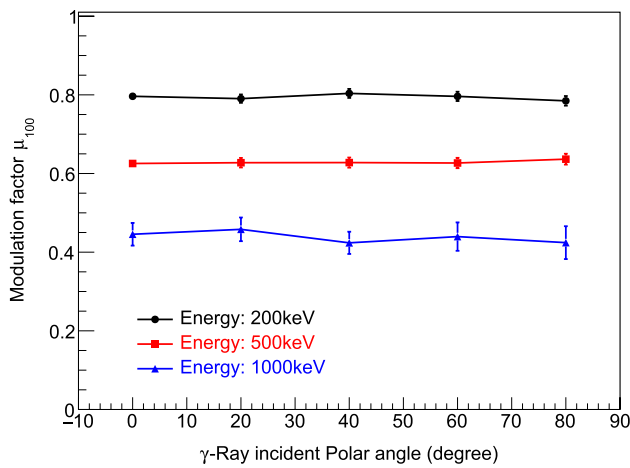


Fig. 12 (Color online) Dependence of the modulation factor on the incident polar angle for photons with energies of 200, 500, and 1000 keV

angles, which is consistent with the theoretical results shown in Fig. 3.

Polarized photons with energies of 200, 500, and 1000 keV were simulated to be incident on the polarimeter at five polar angles (0°, 20°, 40°, 60°, and 80°). Subsequently, three curves for the modulation factor versus the incident polar angle were obtained, as shown in Fig. 12. The three relationship curves show that the modulation factor is almost unaffected by off-axis incidence (independent of the incident polar angle of the photon), indicating that the polarimeter can maintain a stable and remarkable polarization response to photons with different incidence angles. Additionally, the results verified that this polarimeter design had a large FoV.

3.2 Polarization response to a Crab-like source

Two Crab-like sources with a fully linearly polarized (100%) gamma-ray beam and an unpolarized (0%) gamma-ray beam (see Sect. 2.4 for detailed parameters) were used in the simulation experiments of on-axis incidence on the polarimeter, provided that all other configurations were the same. A modulation factor of 0.76 ± 0.01 was obtained by fitting the corrected modulation curve generated by 100% linearly polarized photons using Eq. (3). The polarimeter responds well to continuous polarization photon spectra and is sensitive to monoenergetic polarization photon spectra.

Because the polarization degree of the polarized photons emitted by cosmic gamma-ray sources may sometimes be partially polarized, it is necessary to study the polarization response of the polarimeter to photons with different polarization degrees. The simulated modulation factor μ (see Eq. 4) and simulated polarization degree P (see Eq. 5) were obtained by illuminating the polarimeter with photon beams emitted by Crab-like sources with different degrees

Table 3 Simulated modulation factor μ (see Eq. 4) and simulated polarization degree P (see Eq. 5) for the different polarization degrees of the incident photons from Crab-like sources

Crab-like source polarization degree setup	Polarization degree P simulated	Modulation factor μ simulated
1	1.00 ± 0.02	0.76 ± 0.01
0.8	0.80 ± 0.02	0.61 ± 0.01
0.6	0.59 ± 0.02	0.45 ± 0.01
0.4	0.39 ± 0.01	0.30 ± 0.01
0.2	0.20 ± 0.01	0.15 ± 0.01
0.1	0.09 ± 0.01	0.07 ± 0.01

of polarization (1.0, 0.8, 0.6, 0.4, 0.2, and 0.1). The simulation results for the two polarization parameters are listed in Table 3. From the data in the first and third columns of Table 3, we find that the modulation factor decreases as the polarization degree of the photon decreases, which indicates that the sensitivity of the detector to photons with a small polarization degree decreases; this phenomenon is consistent with the theory. Further, the data in the first and second columns of Table 3 show that the simulated polarization degrees are in good agreement with the actual set polarization degrees within the error tolerance. Therefore, the polarimeter can preserve or accurately recover the polarization degree of the incident photons.

MDP can be defined using Eq. (6) and characterizes the minimum polarization that a polarimeter can detect. When the Crab-like source and background components were used for the simulation experiments of the polarimeter, the relationship curve between $MDP@3\sigma$ and the observation time was obtained. As shown in Fig. 13, the polarization detection capability of the polarimeter increased with the

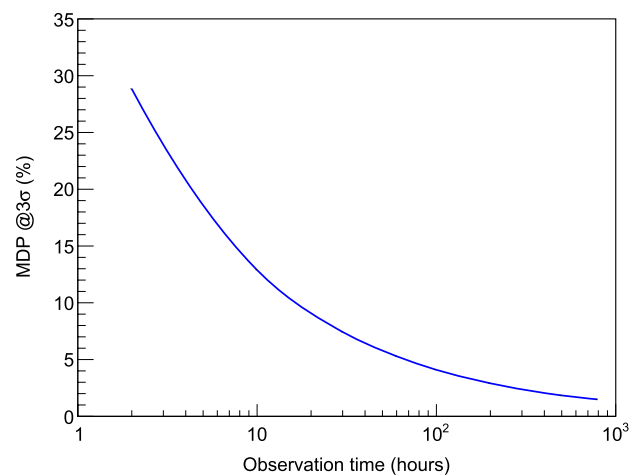


Fig. 13 MDP of the polarimeter for a Crab-like source as a function of the observation time

observation time. During the 24-h observation period, the $MDP@3\sigma$ of the polarimeter was 8.2%. When the observation time reached 10^6 s (~ 277.8 h), the polarimeter detected a 2.4% polarized Crab-like source. In conclusion, the polarimeter with an excellent polarization detection capability can be used to detect the polarization information of soft gamma rays in space to study various astronomical sources.

4 Summary

Cosmic gamma-ray polarization can help explain various astrophysical phenomena and mechanisms from a unique perspective; however, it is not easy to measure. Currently, there are no effective dedicated soft-gamma-ray polarimeters that operate in orbit. Small satellite technology is developing rapidly and has unique advantages over traditional large satellites. Therefore, developing a high-performance dedicated space soft-gamma-ray polarimeter is necessary. The idea of using a constellation of multiple microsatellites to detect the polarization of gamma rays in space is promising. In this study, we investigated a microsatellite in detail. First, a novel structure was designed that included a multi-layer double-sided silicon strip converter in the upper part of the detector, a pixel-type CsI array absorber on five sides excluding the upper side of the converter, and a plastic scintillator ACS on the outermost side. Then, the mass model of the polarimeter was constructed and simulated in detail by setting the performance parameters of each subdetector, different gamma-ray polarization sources, and background components using dedicated simulation software based on the Monte Carlo method. For 100%-polarized photons with an energy of 200 keV that were incident on-axis, the polarimeter achieved a modulation factor of 0.80 ± 0.01 . The modulation factor of the polarimeter showed little dependence on the photon incidence direction. Additionally, the polarimeter precisely measured the polarization angle of the incident photon with an accuracy of 0.2° . For on-axis incident photons in the energy range of 0.1–10 MeV from a Crab-like polarization source, the polarization response of the polarimeter remained remarkable, with a modulation factor of 0.76 ± 0.01 (100% polarization), and the polarization degree of the incident photons was accurately measured with a maximum error of 0.02. Simultaneously, the polarimeter exhibited excellent polarization sensitivity, and the $MDP@3\sigma$ of the polarimeter reached 2.4% after exposure for 10^6 s. Undeniably, the outstanding performance of the polarimeter depends, to some extent, on its wide FoV ($\sim 2\pi$ sr) and potent background suppression. Additionally, the polarimeter simulation results show that the polarimeter response is most pronounced at lower energies and medium scattering angles, which is in good agreement with the theory.

In summary, the use of microsatellites for the detection soft-gamma-ray polarization is promising and can provide new ideas for future space exploration. The novel proposed polarimeter showed excellent polarization detection capability after being verified by simulation experiments; thus it shows great potential for the future task of soft-gamma-ray polarization detection in space. The configuration design of the polarimeter and the simulation methods and results lay a solid foundation for the development of future polarization detection satellite prototypes, promote the smooth development of future constellation programs, and provide a valuable reference for the design of other polarization detectors.

Author Contributions All authors contributed to the study conception and design. Material preparation, data collection, and analysis were performed by Xiang-Man Liu and Shu-Wen Tang. The first draft of the manuscript was written by Xiang-Man Liu, and all authors commented on previous versions of the manuscript. All authors read and approved the final manuscript.

Data Availability The data that support the findings of this study are openly available in Science Data Bank at <https://www.doi.org/10.57760/sciencedb.j00186.00233> and <https://cstr.cn/31253.11.sciencedb.j00186.00233>.

Declarations

Conflict of interest The authors declare that they have no competing interests.

References

1. R. Mignani, A. Shearer, A. Slowikowska et al., *Astronomical Polarisation from the Infrared to Gamma Rays* (Springer, Cham, 2019), pp.109–111
2. S. Komura, A. Takada, Y. Mizumura et al., Imaging polarimeter for a sub-MeV gamma-ray all-sky survey using an electron-tracking Compton camera. *Astrophys. J.* **839**, 41 (2017). <https://doi.org/10.3847/1538-4357/aa68dc>
3. K. Toma, T. Sakamoto, B. Zhang et al., Statistical properties of gamma-ray burst polarization. *Astrophys. J.* **698**, 1042–1053 (2009). <https://doi.org/10.1088/0004-637X/698/2/1042>
4. V. Tatischeff, A.D. Angelis, C. Gouiffès et al., e-ASTROGAM mission: a major step forward for gamma-ray polarimetry. *J. Astron. Telesc. Inst.* **4**, 011003 (2017). <https://doi.org/10.1117/1.JATIS.4.1.011003>
5. N. Produit, F. Barao, S. Deluit et al., POLAR, a compact detector for Gamma Ray Bursts photon polarization measurements. *Nucl. Instrum. Methods Phys. Res. Sect. A* **550**, 616–625 (2005). <https://doi.org/10.1016/j.nima.2005.05.066>
6. Y.Z. Fan, Interpretation and implications of the non-detection of GeV spectrum excess by the Fermi gamma-ray space telescope in most gamma-ray bursts. *Mon. Not. R. Astron. Soc.* **397**, 1539–1548 (2009). <https://doi.org/10.1111/j.1365-2966.2009.15018.x>
7. A.D. Angelis, V. Tatischeff, I.A. Grenier et al., Science with e-ASTROGAM: a space mission for MeV–GeV gamma-ray astrophysics. *J. High Energy Astrop.* **19**, 1–106 (2018). <https://doi.org/10.1016/j.jheap.2018.07.001>

8. J.D. Schnittman, J.H. Krolik, X-ray polarization from accreting black holes: coronal emission. *Astrophys. J.* **712**, 908–924 (2010). <https://doi.org/10.1088/0004-637X/712/2/908>
9. F. Lei, A.J. Dean, G.L. Hills, Compton polarimetry in gamma-ray astronomy. *Space Sci. Rev.* **82**, 309–388 (1997). <https://doi.org/10.1023/A:1005027107614>
10. H.C. Zhang, C. Diltz, M. Böttcher, Radiation and polarization signatures of 3D multi-zone time-dependent hadronic blazar model. *Astrophys. J.* **829**, 69 (2016). <https://doi.org/10.3847/0004-637X/829/2/69>
11. M. Böttcher, Progress in multi-wavelength and multi-messenger observations of blazars and theoretical challenges. *Galaxies* **7**, 20 (2019). <https://doi.org/10.3390/galaxies7010020>
12. P. Laurent, J. Rodriguez, J. Wilms et al., Polarized gamma-ray emission from the galactic black hole Cygnus X-1. *Science* **332**, 438–439 (2011). <https://doi.org/10.1126/science.1200848>
13. H. Krawczynski, A. Garson, Q. Guo et al., Scientific prospects for hard X-ray polarimetry. *Astropart. Phys.* **34**, 550–567 (2011). <https://doi.org/10.1016/j.astropartphys.2010.12.001>
14. M.C. Weisskopf, E.H. Silver, H.L. Kestenbaum et al., A precision measurement of the X-ray polarization of the Crab Nebula without pulsar contamination. *Astrophys. J.* **220**, L117–L121 (1978). <https://doi.org/10.1086/182648>
15. M.L. McConnell, J.M. Ryan, D.M. Smith et al., RHESSI as a hard X-ray polarimeter. *Sol. Phys.* **210**, 125–142 (2002). <https://doi.org/10.1023/A:1022413708738>
16. M. Forot, P. Laurent, I. Grenier et al., Polarization of the crab pulsar and nebula as observed by the INTEGRAL/IBIS telescope. *Astrophys. J. Lett.* **688**, L29–L32 (2008). <https://doi.org/10.1086/593974>
17. D. Yonetoku, T. Murakami, S. Gunji et al., Detection of gamma-ray polarization in prompt emission of GRB 100826a. *Astrophys. J. Lett.* **743**, L30 (2011). <https://doi.org/10.1088/2041-8205/743/2/L30>
18. H.L. Xiao, Y.W. Dong, B.B. Wu et al., POLAR gamma ray burst polarimeter onboard TG-2 Spacelab. *Manned Spacefl.* **21**, 32–36+43 (2015). <https://doi.org/10.3969/j.issn.1674-5825.2015.01.006>. (in Chinese)
19. V. Bhalerao, D. Bhattacharya, A. Vibhute et al., The cadmium zinc telluride imager on AstroSat. *J. Astrophys. Astron.* **38**, 31 (2017). <https://doi.org/10.1007/s12036-017-9447-8>
20. Y. Kishimoto, S. Gunji, Y. Ishigaki et al., Basic performance of PHENEX: a polarimeter for high energy X rays. *IEEE Trans. Nucl. Sci.* **54**, 561–566 (2007). <https://doi.org/10.1109/TNS.2007.897827>
21. S. Larsson, M. Pearce, PoGO: the polarised gamma-ray observer. *Nucl. Instrum. Methods Phys. Res. Sect. A* **525**, 148–152 (2004). <https://doi.org/10.1016/j.nima.2004.03.036>
22. M. Friis, M. Kiss, V. Mikhalev et al., The PoGO+ balloon-borne hard X-ray polarimetry mission. *Galaxies* **6**, 30 (2018). <https://doi.org/10.3390/galaxies6010030>
23. P.F. Bloser, J.S. Legere, J.R. Macri et al., GRAPE—a balloon-borne gamma-ray polarimeter experiment. *Chin. J. Astron. Astrophys.* **6**, 393–397 (2006). <https://doi.org/10.48550/arXiv.astro-ph/0508314>
24. T. Satoru, A. Shigeki, K. Keiki et al., GRAINE project: the first balloon-borne, emulsion gamma-ray telescope experiment. *Prog. Theor. Exp. Phys.* **2015**, 43H01 (2015). <https://doi.org/10.1093/ptep/ptv046>
25. P.F. Bloser, J.M. Ryan, M.L. McConnell et al., The MEGA project: science goals and hardware development. *New Astron. Rev.* **50**, 619–623 (2006). <https://doi.org/10.1016/j.newar.2006.06.001>
26. J.-L. Chiu, S.E. Boggs, H.-K. Chang et al., The upcoming balloon campaign of the compton spectrometer and imager (COSI). *Nucl. Instrum. Methods Phys. Res. Sect. A* **784**, 359–363 (2015). <https://doi.org/10.1016/j.nima.2014.11.099>
27. X. Wen, X.W. Zhang, Analysis of current developments in the field of modern small satellites. *Journal of Shenyang Aerospace University* **30**, 33–36+46 (2013). <https://doi.org/10.3969/j.issn.2095-1248.2013.05.007>. (in Chinese)
28. Z.G. Bai, Development achievements and prospects of China modern small satellite. *Spacecr. Eng.* **28**, 1–8 (2019). <https://doi.org/10.3969/j.issn.1673-8748.2019.02.001>. (in Chinese)
29. J.X. Wen, X.T. Zheng, J.D. Yu et al., Compact CubeSat gamma-ray detector for GRID mission. *Nucl. Sci. Technol.* **32**, 107–117 (2021). <https://doi.org/10.1007/S41365-021-00937-4>
30. O. Engvold, J.-C. Vial, A. Skumanich, *The Sun as a Guide to Stellar Physics* (Elsevier, Amsterdam, 2019), p.189
31. W.F. Liu, X.M. Liu, S.W. Tang et al., Study of the detection unit of the calorimeter for the next generation Compton telescope. *Nucl. Tech.* **43**, 20–28 (2020). <https://doi.org/10.11889/j.0253-3219.2020.hjs.43.010203>. (in Chinese)
32. V. Bindi, A.D. Guerra, G. Levi et al., Preliminary study of silicon photomultipliers for space missions. *Methods Phys. Res. Sect. A* **572**, 662–667 (2007). <https://doi.org/10.1016/j.nima.2006.12.011>
33. X.M. Liu, S.W. Tang, W.F. Liu et al., Study of the γ -Ray Detector of Dual-ended Readout Based on SiPM. *Nuclear Physics Review* **37**, 757–764 (2020). <https://doi.org/10.11804/NuclPhysRev.37.2019CNPC03>. (in Chinese)
34. A. Zoglauer, R. Andritschke, F. Schopper, MEGALib—the medium energy gamma-ray astronomy library. *New Astron. Rev.* **50**, 629–632 (2006). <https://doi.org/10.1016/j.newar.2006.06.049>
35. R. Brun, F. Rademakers, ROOT—an object oriented data analysis framework. *Nucl. Instrum. Methods Phys. Res. Sect. A* **389**, 81–86 (1997). [https://doi.org/10.1016/S0168-9002\(97\)00048-X](https://doi.org/10.1016/S0168-9002(97)00048-X)
36. S. Agostinelli, J. Allison, K. Amako et al., Geant4—a simulation toolkit. *Nucl. Instrum. Methods Phys. Res. Sect. A* **506**, 250–303 (2003). [https://doi.org/10.1016/S0168-9002\(03\)01368-8](https://doi.org/10.1016/S0168-9002(03)01368-8)
37. A.C. Zoglauer, *First Light for the Next Generation of Compton and Pair Telescopes*. Dissertation for the Doctoral Degree (Technical University of Munich, Munich, 2005), pp. 41–125
38. R. Rando, The all-sky medium energy gamma-ray observatory. *J. Instrum.* **12**, C11024 (2017). <https://doi.org/10.1088/1748-0221/12/11/C11024>
39. V. Schönfelder, The imaging gamma-ray telescope COMPTEL aboard GRO. *Adv. Space Res.* **11**, 313–322 (1991). [https://doi.org/10.1016/0273-1177\(91\)90183-K](https://doi.org/10.1016/0273-1177(91)90183-K)
40. S.E. Boggs, The advanced Compton telescope mission. *New Astron. Rev.* **50**, 604–607 (2006). <https://doi.org/10.1016/j.newar.2006.06.076>
41. K. Kamiya, *Compton Recoil Electron Tracking With the TIGRE Gamma-Ray Balloon Experiment*. Dissertation for the Doctoral Degree (University of California, Riverside, Riverside, 2011), pp. 53–61
42. M. Galloway, A. Zoglauer, S.E. Boggs et al., A combined Compton and coded-aperture telescope for medium-energy gamma-ray astrophysics. *A & A* **614**, A93 (2018). <https://doi.org/10.1051/0004-6361/201731122>
43. A. Zoglauer, S.E. Boggs, M. Galloway et al., Design, implementation, and optimization of MEGALib’s image reconstruction tool Mimrec. *A & A* **652**, 568–571 (2011). <https://doi.org/10.1016/j.nima.2010.08.043>
44. P. Cumani, M. Hernanz, J. Kiener et al., Background for a gamma-ray satellite on a low-Earth orbit. *Exp. Astron.* **47**, 273–302 (2019). <https://doi.org/10.1007/s10686-019-09624-0>
45. A. Akyüz, D. Bhattacharya, D.D. Dixon et al., Polarization measurements with an imaging gamma-ray telescope. *Exp. Astron.* **6**, 275–284 (1995). <https://doi.org/10.1007/BF00418325>

46. R. Campana, M. Orlandini, E.D. Monte et al., The radiation environment in a low earth orbit: the case of BeppoSAX. *Exp. Astron.* **37**, 599–613 (2014). <https://doi.org/10.1007/s10686-014-9394-1>
47. M. Tavani, G. Barbiellini, A. Argan et al., The AGILE mission. *Astron. Astrophys.* **502**, 995–1013 (2009). <https://doi.org/10.1051/0004-6361/200810527>

Springer Nature or its licensor (e.g. a society or other partner) holds exclusive rights to this article under a publishing agreement with the author(s) or other rightsholder(s); author self-archiving of the accepted manuscript version of this article is solely governed by the terms of such publishing agreement and applicable law.